

Low-Loss Organic Hyperbolic Materials in the Visible Spectral Range: A Joint Experimental and First-Principles Study

Yeon Ui Lee, Kanghoon Yim, Steven Edward Bopp, Junxiang Zhao, and Zhaowei Liu*

Hyperbolic media strengthen numerous attractive applications in optics such as super-resolution imaging, enhanced spontaneous emission, and nanoscale waveguiding. Natural hyperbolic materials exist at visible frequencies; however, implementations of these materials suffer substantial compromises resulting from the high loss in the currently available candidates. Here, the first experimental and theoretical investigation of regioregular poly(3-alkylthiophenes) (rr-P3ATs), a naturally low-loss organic hyperbolic material (OHM) in the visible frequency range, is shown. These hyperbolic properties arise from a highly ordered structure of layered electron-rich conjugated thiophene ring backbones separated by insulating alkyl side chains. The optical and electronic properties of the rr-P3AT can be tuned by controlling the degree of crystallinity and alkyl side chain length. First-principles calculations support the experimental observations, which result from the rr-P3AT's structural and optical anisotropy. Conveniently, rr-P3AT-based OHMs are facile to fabricate, flexible, and biocompatible, which may lead to tremendous new opportunities in a wide range of applications.

due to the highly directional propagation of volumetrically confined hyperbolic polaritons, which are governed by the complex permittivity tensor of the media. These high-spatial-frequency optical modes play an important role in achieving light manipulation at subdiffraction limited length scales; consequently, HMMs have been widely used in super-resolution imaging,^[12,13] refractive index sensing,^[14] and broadband enhancement of spontaneous emission.^[7,15–18]

At high frequencies, especially the visible frequencies, HMMs often have poor hyperbolic properties for desirable applications. The performance of an HMM can be quantified by the material figure-of-merit ($\text{FoM}_H = -\text{Re}(\epsilon_H)/\text{Im}(\epsilon_H)$, where ϵ_H is the horizontal component of the HMM's complex permittivity^[19]). Optimization of materials choice within the composite is a crucial step in the achievement of reason-

able performance in an HMM. In reality, the maximum spatial frequency supported through a multilayer HMM is limited by fabrication considerations like obtaining ultrafine size in the corresponding unit cell of the multilayer.^[20–22] Moreover, most HMMs are fabricated by multistep processes resulting in composites which suffers from large losses in the constituent metallic layers^[23,24] and at imperfect interfaces. Practically, the optical losses and the finite unit-cell size of a metal/dielectric HMM multilayer set a fundamental upper limit on the maximum spatial frequency. Consequently, there is a clear need to develop a high performance HMM materials platform.

Recently, layered van der Waals crystals have emerged as natural hyperbolic materials, which have phonon-polariton resonances in the IR wavelength range.^[25–27] Naturally hyperbolic materials offer many advantages over traditional HMMs due to their homogeneity, which leads to the generation of extremely high-spatial-frequency modes that are only limited by optical losses.^[21,27] In the visible spectral ranges, only a few materials have been experimentally observed as naturally hyperbolic:^[21] Bi_2Se_3 ,^[28] Bi_2Te_3 ,^[28] and GaTe .^[19] However, they all exhibit a large imaginary part of permittivity and show difficulty in the tuning of their optical properties. Note that Bi_2Se_3 , Bi_2Te_3 , and GaTe have the material figure-of-merit of 2.9, 1.5, and 0.3 at 470, 470, and 497 nm, respectively, which is much smaller than typical metal/dielectric multilayer HMMs.

Recently, layered van der Waals crystals have emerged as natural hyperbolic materials, which have phonon-polariton resonances in the IR wavelength range.^[25–27] Naturally hyperbolic materials offer many advantages over traditional HMMs due to their homogeneity, which leads to the generation of extremely high-spatial-frequency modes that are only limited by optical losses.^[21,27] In the visible spectral ranges, only a few materials have been experimentally observed as naturally hyperbolic:^[21] Bi_2Se_3 ,^[28] Bi_2Te_3 ,^[28] and GaTe .^[19] However, they all exhibit a large imaginary part of permittivity and show difficulty in the tuning of their optical properties. Note that Bi_2Se_3 , Bi_2Te_3 , and GaTe have the material figure-of-merit of 2.9, 1.5, and 0.3 at 470, 470, and 497 nm, respectively, which is much smaller than typical metal/dielectric multilayer HMMs.

Dr. Y. U. Lee, J. Zhao, Prof. Z. Liu
Department of Electrical and Computer Engineering
University of California
9500 Gilman Drive, La Jolla, San Diego, CA 92093, USA
E-mail: zhaowei@ucsd.edu

Dr. K. Yim
Platform Technology Laboratory
Korea Institute of Energy Research
152 Gajeong-ro, Yuseong-gu, Daejeon 34129, Republic of Korea
S. E. Bopp, Prof. Z. Liu
Materials Science and Engineering
University of California
9500 Gilman Drive, La Jolla, San Diego, CA 92093, USA

 The ORCID identification number(s) for the author(s) of this article can be found under <https://doi.org/10.1002/adma.202002387>.

DOI: 10.1002/adma.202002387

An important challenge that must be overcome to fully exploit the useful properties of naturally hyperbolic media is the development of low-loss, practical hyperbolic materials at visible frequencies. Recent studies of organic films made by the solution-processing method have shown strong Lorentz-type optical dispersions including a negative real part of permittivity from molecular conformation and strong intermolecular interactions.^[29–31] In the case that a transition's oscillator strength is sufficiently large, the maximal $\text{Im}(\epsilon) \gg 1$, $\text{Re}(\epsilon)$ can become negative. Since $\text{Im}(\epsilon)$ decays faster than $\text{Re}(\epsilon)$, as frequency is tuned away from resonance, there can exist an off-resonance frequency range over which $\text{Re}(\epsilon)$ is negative and $\text{Im}(\epsilon)$ is small.^[29–31] Thus, organic films exhibiting these specific optical properties are likely to be attractive substitutes for metals at visible frequencies. Additionally, organic films offer many other advantages such as light weight, low cost, mechanical flexibility, facile solution-based processing at a large scale, highly tunable optoelectronic properties,^[32] excellent biocompatibility,^[33,34] and support of various surface functionalizations^[35] for biological and biochemical applications. However, hyperbolic optical properties from organic materials in the visible frequencies have not been reported up to now.

In this study, we show for the first time that self-assembled regioregular films of poly(3-alkylthiophenes) (rr-P3ATs) are tunable organic hyperbolic materials (OHMs) with ultra-subwavelength unit cells and relatively low-loss in visible frequencies. We show with theory and experiment that the effective conjugation chain length and alkyl chain length of rr-P3ATs have a tremendous effect on hyperbolic dispersion resulting from differences in the degrees of anisotropic crystallinity between distinctly prepared films. Control of the anisotropic crystallinity is essential for obtaining a hyperbolic dispersion in rr-P3AT films. We use variable angle spectroscopic ellipsometry (VASE) analysis to characterize optical properties of the films. Good agreement between VASE, grazing-incidence X-ray diffraction (GIXD) measurement, and the results of first-principles calculations indicates that the rr-P3AT films support a tunable hyperbolic response in the visible frequency range. The best material figure-of-merit around 18 at 465 nm, makes OHMs an outstanding hyperbolic material in the visible spectrum.

All polymers belonging to the P3AT family consist of electron-rich conjugated backbones built of thiophene rings and insulating alkyl side chains ($\text{C}_n\text{H}_{2n+1}$).^[36] Figure 1a shows the chemical structure of regioregular poly(3-hexylthiophene-2,5-diyl) (rr-P3HT): a member of the rr-P3AT family having its 3-position occupied on the thiophene ring in the monomer, and hexyl ($n = 6$) side chains. To produce a range of distinct crystalline structures^[37] in the rr-P3HT films, 10, 40, 60, 80, and 100 mg portions of >98% regioregular head-to-tail P3HT (Sigma-Aldrich, average $M_w \approx 87\,000\text{ g mol}^{-1}$) were each dissolved in 1 mL portions of chlorobenzene (CB). The resulting solutions were heated at 50 °C for 3 h (P3HT:CB = 10, 40, 60, 80, and 100 mg mL⁻¹; Figure 1b). P3HT:CB solutions were spin-coated onto plasma-cleaned glass substrates (see the Experimental Section for details of the OHM film fabrication) to form thin polymer films. Film thicknesses (28, 82, 120, 145, and 182 nm, respectively) were measured by both a DekTak surface profilometer and VASE. VASE was also used to determine the permittivity spectra of the films (see the Experimental Section

for details of the VASE measurement). Figure 1b shows photographs of the samples indicating a range of metallicity in the visible region of rr-P3HT films having different concentrations.

Figure 1c shows that the horizontal H - and vertical z -components of the complex permittivity, obtained from the VASE measurement using an anisotropic model, are strongly influenced by polymer solution concentration. By increasing the concentration, a clear red-shift of the intrachain π - π^* transition,^[38] and increased transition strengths are observed. For the high concentration rr-P3HT films (60, 80, and 100 mg mL⁻¹), strong dispersions take place along the H -axis and relatively weak dispersion was observed along the z -axis, which leads a type-II hyperbolic dispersion ($\epsilon_H < 0$ and $\epsilon_z > 0$) in the 400–560 nm spectral range (the green-colored region in Figure 1c). The strong optical anisotropy between the horizontal and vertical directions (with respect to the substrate plane) indicates that the high concentration rr-P3HT films have a uniaxial lamellar crystalline structure (Figure 1d) with 2D conjugated sheets of π -stacked polythiophene backbones separated by layers of the alkyl side-chains. According to the literature, interchain distance d is around 16 Å^[39–41] which will be explored in the next section. Unlike the (001) direction, charge transfer along (100) is prevented by the alkyl side chains which have an insulating effect. It is clear that such highly anisotropic charge transport affects the optical properties; resultantly, those charge transport properties may be manipulated to achieve hyperbolic dispersion in highly ordered rr-P3HT films. Figure 1e–g shows calculated equipfrequency contours for the 10 mg mL⁻¹ (Figure 1e), 60 mg mL⁻¹ (Figure 1f), and 100 mg mL⁻¹ (Figure 1g) rr-P3HT films at a wavelength of 500 nm, from which elliptical (Figure 1e) and hyperbolic shapes (Figure 1f,g) are clearly obtained.

Here, we claim that the experimental results are indicative of concentration-dependence in the optical dispersion of the rr-P3HT films resulting from modifications to their effective conjugation chain length (degree of conjugation). Conjugation chains of rr-P3HTs with a molecular weight of ≈ 87 kDa (Table S1, Supporting Information) are long enough (≈ 545 repeating monomer units, ≈ 406 nm)^[42,43] to fold back on themselves many times. In addition to the chain-folding, backbone torsion and conjugation breakages regulate the effective conjugation chain length, crystallinity, and optical dispersion of the rr-P3HT films. An increase of aggregations and interactions between adjacent thiophene backbone rings leads to a planarization of the thiophene backbones,^[44,45] resulting in a larger π -orbital overlap along first-nearest-neighbor backbones, a longer effective conjugation length, and larger degree of anisotropic crystallinity. Therefore, a strong transition dipole moments arise from the electron-rich in-plane excitons as compared to the out-of-plane excitons in the high concentration rr-P3HT films. Alternatively, in the films having lower rr-P3HT concentrations, molecules can cause local nonplanarity^[46] including chain folding/ending^[37] and deuteration^[47] of the thiophene rings, weakening the π -conjugation along the polymer backbone; interchain interactions are also significantly reduced.

To verify the connection between effective conjugation chain length and concentration-dependent complex permittivity of rr-P3HT films, optical properties of crystalline rr-P3HTs are investigated with density functional theory (DFT) calculations.

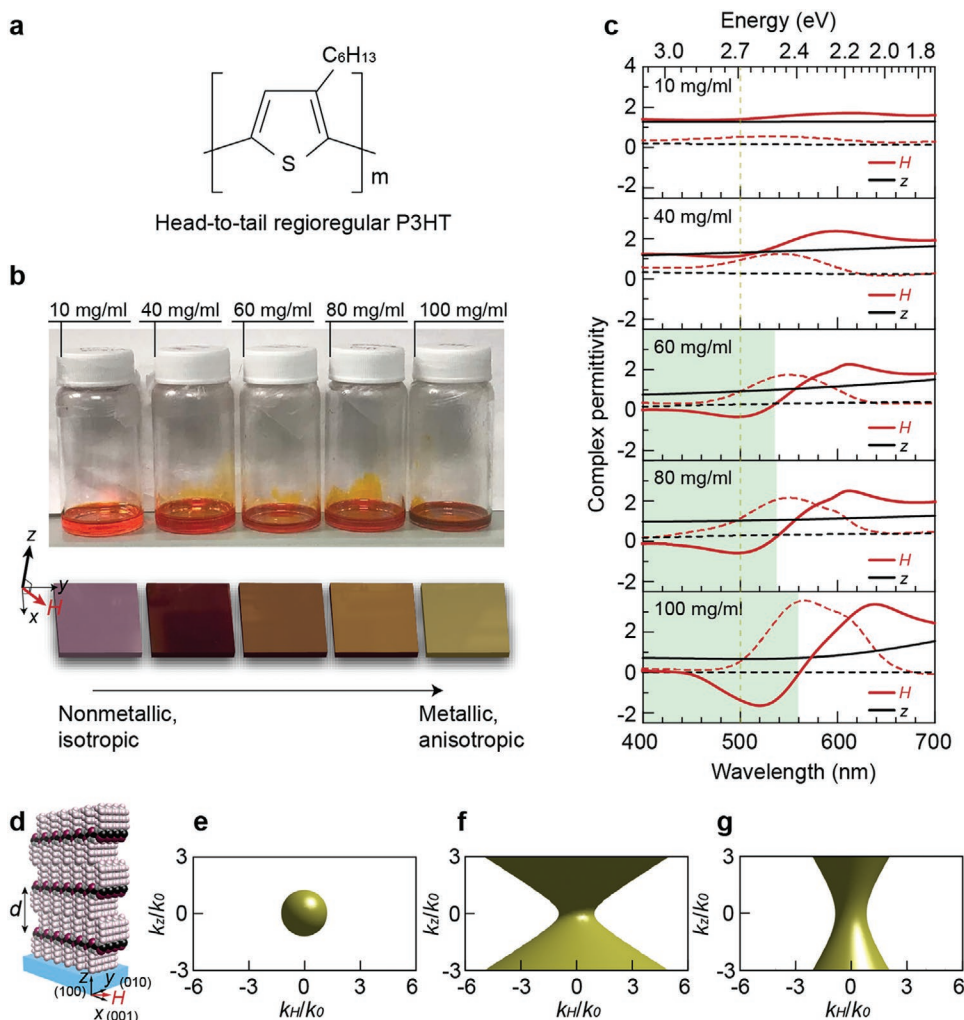


Figure 1. a) Chemical structures of rr-P3HT. b) Photographs of 10, 40, 60, 80, and 100 mg mL⁻¹ concentration rr-P3HT:CB solutions and spin-coated films on glass substrates. c) Horizontal *H*- (red curves) and vertical *z*- (black curve) components of real (solid curve) and imaginary (dashed curve) parts of the complex permittivity of rr-P3HT films ranging from a low-concentration (10 mg mL⁻¹, top) to a high-concentration (100 mg mL⁻¹, bottom). d) A schematic representation of the crystalline structure for an rr-P3HT film. e–g) Equipfrequency contours of the 10 mg mL⁻¹ (e), 60 mg mL⁻¹ (f), and 100 mg mL⁻¹ (g) rr-P3HT films at $\lambda = 500$ nm.

The oligomer conformations of isolated polythiophene backbones (e.g., (3HT)_{*m*} oligomers containing *m*-monomer units) are adopted and assumed to correspond to the effective conjugation chains of rr-P3HT films. The crystalline configurations of the (3HT)_{*m=2,4,6*} oligomers and P3HT (= (3HT) _{∞}) are shown in **Figure 2a**. Calculated lattice parameters of the optimized P3HT unit-cell (dashed red box in **Figure 2a**) were $a = 7.8$ Å, $b = 5.2$ Å, $c = 15.0$ Å, and $\alpha = \beta = \gamma = 90^\circ$ which are consistent with previous reports^[40,48–50] (see computational details in the Experimental Section).

By comparing computed *m*-dependent complex permittivity and experimental results, one can easily identify a relationship between effective conjugation chain lengths and rr-P3HT concentrations in the films. **Figure 2b** shows the calculated complex permittivity of (3HT)_{*m*} oligomers. The imaginary part of permittivity is shown with a dashed curve, and the real part, calculated by the Kramers–Kronig transformation, is shown with a solid curve. Since calculated permittivity does not contain

information on the average distribution of local packing orientation, biaxial permittivity (asymmetric in-plane, $\epsilon_x \neq \epsilon_y$) is shown in **Figure 2b**. In the case of spin-coated films, the symmetry of the system is higher than that of the underlying crystal due to the averaging of local packing orientation distribution.^[51] Thus, the measured permittivity is uniaxial (symmetric in-plane, $\epsilon_x = \epsilon_y \equiv \epsilon_H$) with *c* (*z*)-axis along the surface normal.

As shown in the *x*-component of the imaginary part of permittivity (dashed red curve), the center peak wavelength of $\text{Im}(\epsilon_x)$ shifts toward longer wavelengths when the effective conjugation length, *m* is increased. We observe that the optical transition along the conjugation-backbone direction (001) is the most significant at the band edge. A gap between the highest occupied molecular orbital (HOMO) and lowest unoccupied molecular orbital (LUMO) becomes smaller when the conjugation chain length increases (see Table S2 and **Figure S2** in the Supporting Information). Note that the center peak wavelengths of $\text{Im}(\epsilon_x)$ for the $m \geq 5$ monomer units are close to the

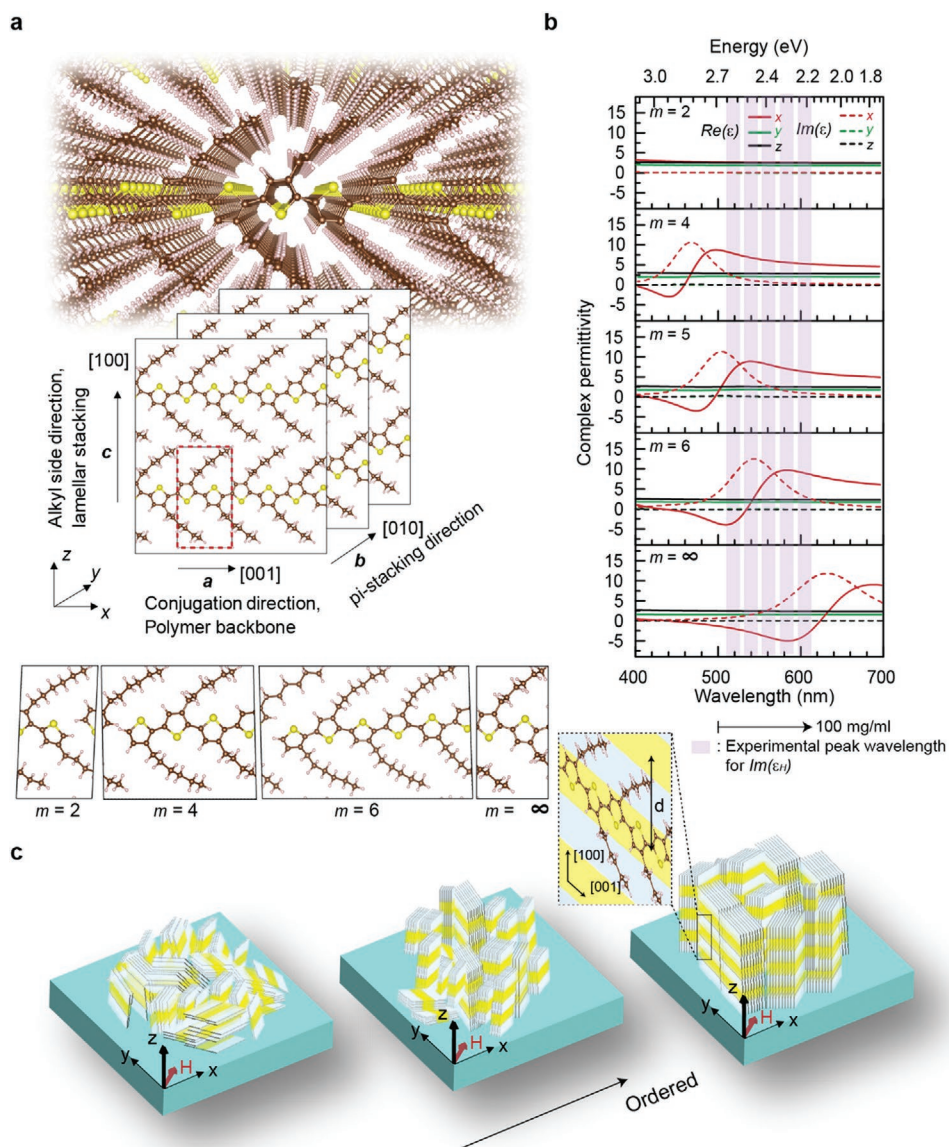


Figure 2. DFT methods used to investigate the optical hyperbolic dispersion of rr-P3HT structures. a) Conventional unit cells are represented for the $(3HT)_{m=2,4,6}$ oligomers and P3HT ($= (3HT)_{\infty}$). S, C, and H atoms are represented as yellow, brown, and light pink, respectively. b) Calculated complex permittivity of the $(3HT)_m$ for the horizontal (x: red curve; y: green curve) and vertical (z: black curve) components of the optical transition. c) Schematic of possible crystal packing arrangements (not to scale) within a set of rr-P3HT films having different effective conjugation lengths and degrees of ordering. Conjugation backbones are marked with yellow, and insulating hexyl chains are marked with light gray.

experimental values for rr-P3HT films (the pink-colored region in Figure 2b). A higher ordering of rr-P3HT molecules can lead to a longer effective conjugation chain length and a redshift of hyperbolic dispersion range.

Figure 2c compares the schematics of possible crystal packing arrangements (not to scale) present in rr-P3HT films with different orders of crystallinity. A lower concentration film shows a large number of small domains containing more insulating grain boundaries in the horizontal plane. High concentration films, however, have few insulating grain boundaries in the horizontal plane. As deduced from the above study of experimental and calculated optical dispersion spectra, results indicate that oligomer chains are increasingly aligned and

make longer effective conjugation chains in higher concentration films, which have hyperbolic dispersion.

To confirm the concentration-dependent crystallinity of rr-P3HT, we perform GIXD analysis. In the GIXD measurement (Figure 3a), a (100) peak corresponding to the interchain distance in the stacking direction indicates lamellar organization which corresponds to the identity distance along the c -axis direction (unit cell periodicity of ≈ 1.63 nm) of crystalline where (100) peak strength is correlated with an increasing discretization of molecules into ordered layers along the c -axis. This identity distance was calculated from Bragg's law. GIXD results for the high concentration film (100 mg mL^{-1}) show a (100) peak indicating a high degree of layering in its crystalline structure.

By decreasing concentration, peak intensity of the interchain distance becomes weaker, resulting from an increase of disordered interlamellar zones containing the chain folds, as well as the chain ends causing a change in molecular tilt angle (i.e., degree of chain interdigitation).

In Figure 3b, GIXD results for the 100 mg mL⁻¹ rr-P3HT film shows a sharp (100) peak, caused by an increase in preferred orientation of crystallites in the films after annealing at 170 °C for 20 min. The annealing-induced recrystallization led to a substantial increase in overall crystallinity of the material, and a stronger alignment of the crystals in comparison to as-cast films. Insets in Figure 3b compare qualitative schematics of crystalline structures present in the films before and after annealing. After annealing, highly oriented crystals organize in the films and the total number of insulating grain boundaries in the horizontal plane decreases. Figure 3c shows a comparison of the complex permittivity in the 100 mg mL⁻¹ rr-P3HT films before and after annealing. Increasing optical anisotropy is caused by an increase in the total degree of preferred orientation in the crystal after annealing.

Here, we describe the influence of alkyl side chain length in the rr-P3AT crystal on its optical properties. Chemical structures of rr-P3ATs having different alkyl side chains (C_nH_{2n+1}, *n* = 6, 8, 10) are shown in Figure 4a, namely, poly(3-hexylthiophene) (P3HT), poly(3-octylthiophene) (P3OT), and poly(3-decylthiophene) (P3DT). In general, increasing the alkyl chain length has the potential to reduce oscillator strength^[52] because the alkyl chain regions are insulating and do not contribute to optical absorption in the visible range. Alternatively, the presence of longer alkyl groups can cause local non-planarity^[53] (chain folding/ending) leading to a shorter effective chain conjugation length, which weakens π -conjugation along the

polymer backbone and blueshifts the resonance wavelength. Therefore, for the rr-P3ATs with longer alkyl side chains, the horizontal component of permittivity provides a dispersive response at shorter wavelengths; spectral tuning of the hyperbolic dispersion in the visible spectral range is thereby possible.

GIXD analysis of P3AT films for three different alkyl chain lengths (Figure 4b) shows a peak at $2\theta = 5.4^\circ$ for rr-P3HT, $2\theta = 4.3^\circ$ for rr-P3OT, and $2\theta = 3.6^\circ$ for rr-P3DT, which correspond to the interchain spacing distances $d = 1.63$, 2.05, and 2.45 nm, respectively. An increase in side chain length clearly induces larger interchain spacing. Figure 4c shows the measured complex permittivity spectra of the 100 mg mL⁻¹ rr-P3AT films (see the Experimental Section for details of the OHM film fabrication). We observe a decrease of dispersion in Re(ϵ_z) and Im(ϵ_H), and the Im(ϵ_H) peaks blueshift with an increase in the alkyl chain length of the rr-P3ATs. This phenomenon can be explained by two factors. First, longer alkyl side chains cause roughening and an increasing insulating volume between the polymer domains and reduces the oscillator strength. Second, the phenomenon can be also attributed to local nonplanarity which leads shortening of effective conjugation chain length m (disturbance in the polymer chain packing in the presence of long alkyl chains, i.e., distortion in the polymer stacking^[53]). DFT calculations of crystalline rr-P3ATs (Figure S3, Supporting Information) consistently show that increasing the length of the alkyl chains reduces oscillator strength along the horizontal direction. Since the calculation results of crystalline rr-P3ATs do not show a blueshift with different alkyl chain length, the experimentally observed peak shift should be explained by taking account of different effective conjugation lengths m . This tunability allows for a high material figure-of-merit

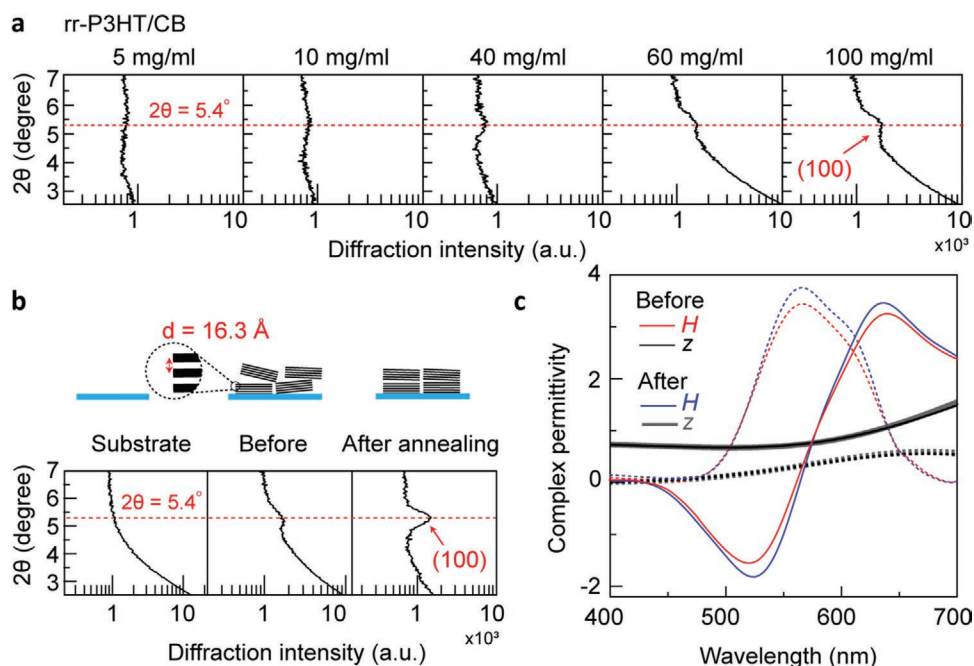


Figure 3. a) Grazing incidence X-ray diffractograms of rr-P3HT films with different concentrations (5, 10, 40, 60, and 100 mg mL⁻¹). b) GIXD on a sapphire substrate of rr-P3HT films before and after annealing at 170 °C for 20 min. Inset: Schematics of the crystalline lamellar structure before and after annealing. c) Horizontal *H*- and vertical *z*-components of real (solid curve) and imaginary (dashed curve) parts of the complex permittivity of rr-P3HT film before annealing (red and black curves) and after annealing (blue and gray curves).

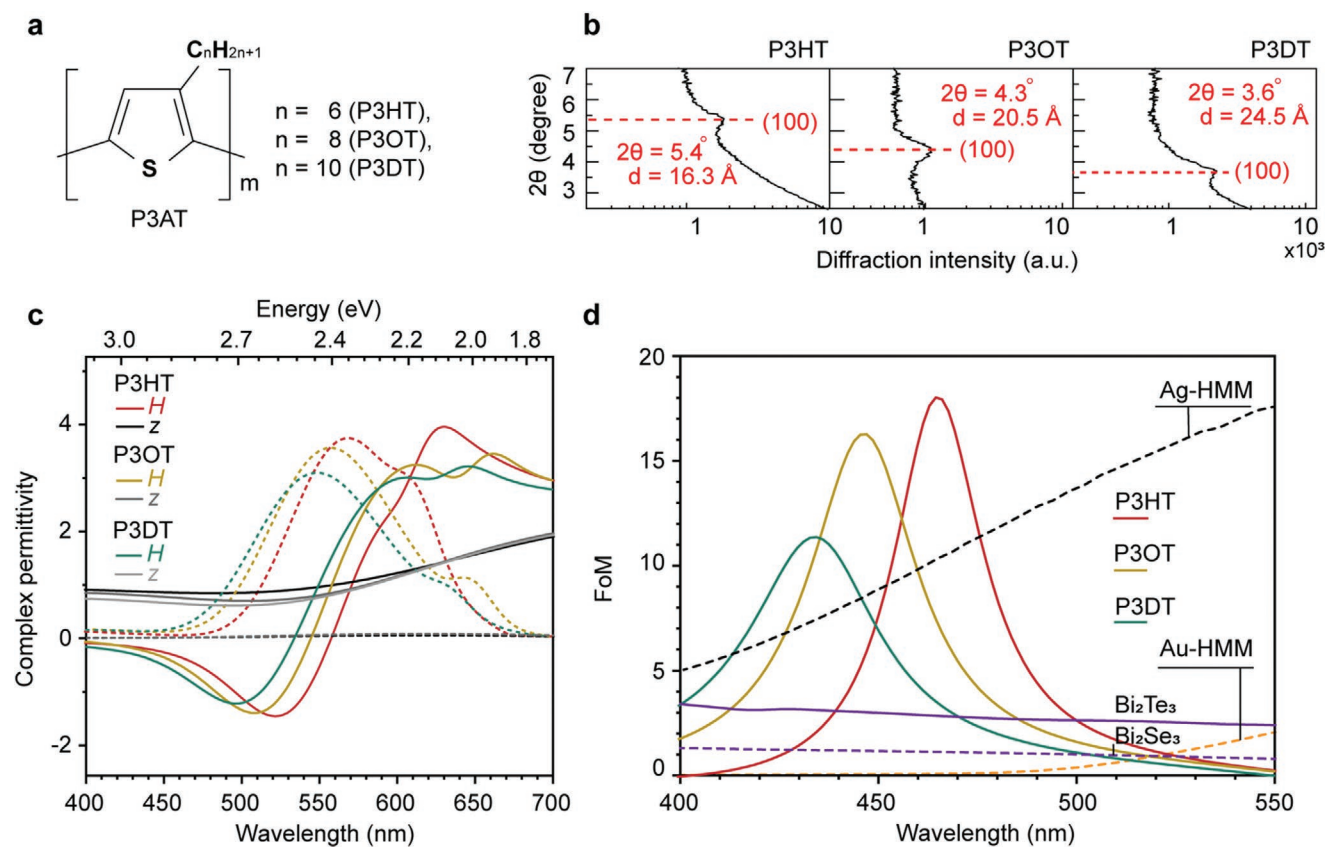


Figure 4. Hyperbolic dispersion of rr-P3ATs in terms of alkyl side chain length. a) Chemical structures of the rr-P3ATs having different alkyl side chains. b) Grazing-incidence X-ray diffractograms of rr-P3AT films. c) Measured complex permittivity of the rr-P3AT films. d) Figure-of-merit ($FOM_H = -\text{Re}(\epsilon_H)/\text{Im}(\epsilon_H)$) for the rr-P3ATs, Ag-based HMM formed by the effective medium approximation of alternating layers of Ag/SiO₂ with a metal filling fraction of 50% (FOM_H of the Ag-based HMM was calculated using data from ref. [55]), Au-based HMM formed by the effective medium approximation of alternating layers of Au/SiO₂ with a metal filling fraction of 50% (FOM_H of the Au-based HMM was calculated using data from ref. [56]), Bi₂Se₃, and Bi₂Te₃ (FOM_H of the tetradymite was calculated using data from ref. [28]).

($FOM_H = -\text{Re}(\epsilon_H)/\text{Im}(\epsilon_H)$) (Figure 4d), maximum high-spatial-frequency of hyperbolic polariton modes, allowing for optimized super-resolution imaging applications at various operational wavelengths. The OHM outperforms traditional hyperbolic materials in the visible spectrum (Figure 4d).

We now describe the important findings to provide new insight into OHMs operating in the visible frequency range as an attractive replacement for metal-based HMMs. Even though many promising HMM-based applications operate nicely within the visible spectral range, their performance is limited by their finite unit cell size and optical losses.^[23,54–56] In Figure 4d, HMM composed of alternating layers of 20 nm thick Ag (Au)/SiO₂ with a metal filling fraction of 50% shows much lower FOM_H than that of OHMs. Unlike the 3D charge transport of metals in traditional inorganic multilayer HMMs, charge transport in an OHM—which relies on π -orbital overlap between adjacent chains (see Section S3 in the Supporting Information)—is itself anisotropic. The OHM provides a homogeneous Lorentz-type hyperbolic dispersion and low-loss hyperbolic polariton modes, which make OHMs an outstanding hyperbolic material in the visible spectrum. Compared to inorganic multilayer HMMs, the OHMs not only provide a better material figure-of-merit in visible spectral range but also offer many other advantages such

as light weight, low expense, mechanical flexibility, facile solution processing at a large scale, highly tunable optoelectronic properties,^[32] excellent biocompatibility,^[33,34] and support of various surface functionalizations^[35] for bioimaging.

In conclusion, we have fabricated rr-P3AT films that have hyperbolic dispersion at visible frequencies for the first time via a solution process using the spin-coating method. We have performed a combined experimental and theoretical study of the hyperbolic dispersion in these OHM films. We have shown that conjugated polymer films must be assembled with a high degree of crystallinity, indicating a longer effective conjugation length is important to achieve desirable hyperbolic properties at visible frequencies. The alkyl side chain lengths of the rr-P3ATs also play an important role in the stacking arrangement and spectral tuning of the hyperbolic dispersion. This allows clear identification of the crystalline structure and optical property relationships for rr-P3AT films with different crystallographic ordering. Our results suggest that these OHMs can be further utilized as an attractive alternative to the traditional hyperbolic materials operating in the visible frequency range. This study provides a new understanding of hyperbolic dispersion in cost-effective, flexible, and biocompatible materials, which may lead to important applications in various fields like super-resolution bioimaging.

Experimental Section

OHM Film Fabrication: From the head-to-tail 98% regioregular P3HT (molecular weight $M_w \approx 87\,000$ from Sigma-Aldrich), 10, 40, 60, 80, and 100 mg portions were solutionized individually in 1 mL volumes of chlorobenzene and heated to 50 °C for 3 h to ensure total dissolution. Solutions were allowed to rest at room temperature for 2 h, resulting in a series of orange solutions with color saturation directly correlated to solute concentration. Thin films were spin-coated onto 0.17 mm thick cleaned glass coverslips at 5000 rpm for 60 s. Film thicknesses of 28, 82, 120, 145, and 182 nm, respectively, resulted from these fabrications, and were measured either by DekTak surface profiler or variable angle spectroscopic ellipsometry. The head-to-tail 98% regioregular P3OT (molecular weight $M_w \approx 34\,000$, Sigma-Aldrich) and P3DT (molecular weight $M_w \approx 30\,000$, Sigma-Aldrich) were used for the P3OT and P3DT films; these samples were fabricated with the same sample processing as those described for the P3HT films. Film thickness of 172 and 182 nm were measured either by DekTak surface profiler or variable angle spectroscopic ellipsometry (Table S1, Supporting Information).

VASE Measurement: A rotating polarizer-type spectroscopic ellipsometer (J. A. Woollam M-2000D, J. A. Woollam Co., Ltd. having a beam size of 3 mm) was used to obtain the permittivity of the OHMs as a function of photon energy. The measurements were performed in the spectral range of 1.55–4.0 eV (310–800 nm) for 60° and 70° angles of incidence. This approach improves the accuracy of modeling analysis and allows for the determination of film thicknesses and refractive index. The measured ellipsometric constants Ψ and Δ were defined from the ratio of the reflection coefficients r_p and r_s for the p- and s-polarizations, respectively (Figure S1, Supporting Information).

GIXD Measurement: rr-P3HT films were analyzed with 2θ - ω scans of 0.030° step size using Cu-K α radiation and a Ni Cu-K β filter from 0° to 45° in a Panalytical X'Pert X-ray Diffractometer. With the diffractometer in the point-source configuration, a 1° incident beam slit with 1 and 4 mm perpendicular masks were used to shape the X-ray beam, which had been generated at 45 kV and 40 mA onto samples lying on a multipurpose stage. The X-ray system was aligned to a low angle peak in the sapphire substrates at around $2\theta = 9^\circ$. Machine offsets were calculated by comparing this peak position in the 2θ - ω and ω -scan geometries.

DFT Calculations: Vienna Ab initio Simulation Package (VASP)^[57] with projector augmented-wave (PAW) potentials was used for the DFT calculations. The generalized gradient approximation (GGA) was employed for the exchange–correlation functional. The energy cut-off of the plane-wave basis was set to 450 eV and k -point sampling was determined so as to satisfy an energy per atom difference of less than 5 meV, and that forces on cells differ by less than 5 kB. Geometry optimization (cell relaxation) was conducted until atomic forces converged to within 0.01 eÅ⁻¹. To obtain dielectric functions, the frequency-dependent microscopic polarizability matrix was calculated from the electronic ground states.^[58] Here, denser k -point samplings (doubled k -point density compared to structural optimizations) were set for reasonable accuracy. In addition, since using a GGA functional severely underestimates bandgap energies (E_g), a scissor operation was applied to the obtained dielectric function with $\Delta E = E_g^{\text{HSE06}} - E_g^{\text{GGA}}$, where E_g^{HSE06} is the calculated bandgap using HSE06^[59] hybrid functional (0.25 for the fraction of Fock exchange) and E_g^{GGA} is the bandgap calculated by GGA. This approach was adopted to avoid huge computational costs caused by the poor scalability of the hybrid functional.

Supporting Information

Supporting Information is available from the Wiley Online Library or from the author.

Acknowledgements

Y.U.L. and K.Y. contributed equally to this work. This work was supported by the Gordon and Betty Moore Foundation, the National Science

Foundation (CBET1604216), and the Research and Development Program of the Korea Institute of Energy Research (B9-2453). The computation was carried out at the KISTI supercomputing center (KSC-2018-S1-0007).

Note: The author list of ref. [40] was corrected on July 14, 2020, after initial publication online. The caption of Figure 4d relating to FOM_H of the Ag-based HMM, FOM_H of the Au-based HMM, and FOM_H of the tetradymite was also corrected.

Conflict of Interest

The authors declare no conflict of interest.

Keywords

low-loss materials, metamaterials, organic hyperbolic materials, poly(3-alkylthiophenes)

Received: April 7, 2020
Published online: June 3, 2020

- [1] D. R. Smith, J. B. Pendry, M. C. K. Wiltshire, *Science* **2004**, *305*, 788.
- [2] J. B. Pendry, D. Schurig, D. R. Smith, *Science* **2006**, *312*, 1780.
- [3] J. B. Pendry, L. Martín-Moreno, F. J. Garcia-Vidal, *Science* **2004**, *305*, 847.
- [4] L. Ferrari, C. Wu, D. Lepage, X. Zhang, Z. Liu, *Prog. Quantum Electron.* **2015**, *40*, 1.
- [5] Y. Guo, W. Newman, C. L. Cortes, Z. Jacob, *Adv. OptoElectron.* **2012**, *2012*, 452502.
- [6] A. Poddubny, I. Iorsh, P. Belov, Y. Kivshar, *Nat. Photonics* **2013**, *7*, 948.
- [7] P. Shekhar, J. Atkinson, Z. Jacob, *Nano Convergence* **2014**, *1*, 14.
- [8] S. Chen, Z. Li, W. Liu, H. Cheng, J. Tian, *Adv. Mater.* **2019**, *31*, 1802458.
- [9] H. Li, W. Hao, X. Yin, S. Chen, L. Chen, *Adv. Opt. Mater.* **2019**, *7*, 1900493.
- [10] E. Narimanov, *ACS Photonics* **2016**, *3*, 1090.
- [11] Q. Ma, H. Hu, E. Huang, Z. Liu, *Nanoscale* **2017**, *9*, 18268.
- [12] Z. Liu, H. Lee, Y. Xiong, C. Sun, X. Zhang, *Science* **2007**, *315*, 1686.
- [13] J. Sun, M. I. Shalaev, N. M. Litchinitser, *Nat. Commun.* **2015**, *6*, 7201.
- [14] N. Vasilantonakis, G. A. Wurtz, V. A. Podolskiy, A. V. Zayats, *Opt. Express* **2015**, *23*, 14329.
- [15] Z. Jacob, I. I. Smolyaninov, E. E. Narimanov, *Appl. Phys. Lett.* **2012**, *100*, 181105.
- [16] D. Lu, J. J. Kan, E. E. Fullerton, Z. Liu, *Nat. Nanotechnol.* **2014**, *9*, 48.
- [17] H. N. S. Krishnamoorthy, Z. Jacob, E. Narimanov, I. Kretzschmar, V. M. Menon, *Science* **2012**, *336*, 205.
- [18] Z. Jacob, J. Y. Kim, G. V. Naik, A. Boltasseva, E. E. Narimanov, V. M. Shalaev, *Appl. Phys. B* **2010**, *100*, 215.
- [19] K. Korzeb, M. Gajc, D. A. Pawlak, *Opt. Express* **2015**, *23*, 25406.
- [20] B. Wood, J. B. Pendry, D. P. Tsai, *Phys. Rev. B* **2006**, *74*, 115116.
- [21] E. E. Narimanov, A. V. Kildishev, *Nat. Photonics* **2015**, *9*, 214.
- [22] T. Li, V. Nagal, D. H. Gracias, J. B. Khurgin, *Opt. Express* **2017**, *25*, 13588.
- [23] G. V. Naik, A. Boltasseva, *Metamaterials* **2011**, *5*, 1.
- [24] P. B. Johnson, R. W. Christy, *Phys. Rev. B* **1972**, *6*, 4370.
- [25] S. Dai, Z. Fei, Q. Ma, A. S. Rodin, M. Wagner, A. S. McLeod, M. K. Liu, W. Gannett, W. Regan, K. Watanabe, T. Taniguchi, M. Thiemens, G. Dominguez, A. H. Castro Neto, A. Zettl, F. Keilmann, P. Jarillo-Herrero, M. M. Fogler, D. N. Basov, *Science* **2014**, *343*, 1125.
- [26] T. Low, A. Chaves, J. D. Caldwell, A. Kumar, N. X. Fang, P. Avouris, T. F. Heinz, F. Guinea, L. Martín-Moreno, F. Koppens, *Nat. Mater.* **2017**, *16*, 182.

- [27] M. N. Gjerding, R. Petersen, T. G. Pedersen, N. A. Mortensen, K. S. Thygesen, *Nat. Commun.* **2017**, *8*, 320.
- [28] M. Esslinger, R. Vogelgesang, N. Talebi, W. Khunsin, P. Gehring, S. de Zuani, B. Gompf, K. Kern, *ACS Photonics* **2014**, *1*, 1285.
- [29] L. Gu, J. Livenere, G. Zhu, E. E. Narimanov, M. A. Noginov, *Appl. Phys. Lett.* **2013**, *103*, 021104.
- [30] Y. U. Lee, E. Garoni, H. Kita, K. Kamada, B. H. Woo, Y. C. Jun, S. M. Chae, H. J. Kim, K. J. Lee, S. Yoon, E. Choi, F. Mathevet, I. Ozerov, J. C. Ribierre, J. W. Wu, A. D'Aléo, *Adv. Opt. Mater.* **2018**, *6*, 1701400.
- [31] Y. U. Lee, O. P. M. Gaudin, K. Lee, E. Choi, V. Placide, K. Takaishi, T. Muto, P. André, A. Muranaka, M. Uchiyama, F. Mathevet, T. Aoyama, J. Wu, A. D'Aléo, J.-C. Ribierre, *ACS Photonics* **2019**, *6*, 1681.
- [32] J. A. Geldmeier, M. A. Mahmoud, J.-W. W. Jeon, M. El-Sayed, V. V. Tsukruk, *J. Mater. Chem. C* **2016**, *4*, 9813.
- [33] F. Di Maria, F. Lodola, E. Zucchetti, F. Benfenati, G. Lanzani, *Chem. Soc. Rev.* **2018**, *47*, 4757.
- [34] J. Chelora, J. Zhang, R. Chen, H. T. Chandran, C.-S. Lee, *Nanotechnology* **2017**, *28*, 285102.
- [35] C. Bossio, I. Abdel Aziz, G. Tullii, E. Zucchetti, D. Debellis, M. Zangoli, F. Di Maria, G. Lanzani, M. R. Antognazza, *Front. Bioeng. Biotechnol.* **2018**, *6*, 114.
- [36] T. Chen, X. Wu, R. D. Rieke, *J. Am. Chem. Soc.* **1995**, *117*, 233.
- [37] R. Noriega, J. Rivnay, K. Vandewal, F. P. V. Koch, N. Stingelin, P. Smith, M. F. Toney, A. Salleo, *Nat. Mater.* **2013**, *12*, 1038.
- [38] L. Farouil, F. Alary, E. Bedel-Pereira, J. L. Heully, *J. Phys. Chem. A* **2018**, *122*, 6532.
- [39] H. Sirringhaus, P. J. Brown, R. H. Friend, M. M. Nielsen, K. Bechgaard, B. M. W. Langeveld-Voss, A. J. H. Spiering, R. A. J. Janssen, E. W. Meijer, P. Herwig, D. M. de Leeuw, *Nature* **1999**, *401*, 685.
- [40] D. Alberga, A. Perrier, I. Ciofini, G. F. Mangiatordi, G. Lattanzi, C. Adamo, *Phys. Chem. Chem. Phys.* **2015**, *17*, 18742.
- [41] N. Seidler, G. M. Lazzarini, G. Li Destri, G. Marletta, F. Cacialli, *J. Mater. Chem. C* **2013**, *1*, 7748.
- [42] M. L. Jones, D. M. Huang, B. Chakrabarti, C. Groves, *J. Phys. Chem. C* **2016**, *120*, 4240.
- [43] E. Miller, M. Jones, E. Jankowski, *Polymers* **2018**, *10*, 1358.
- [44] S. G. Urquhart, M. Martinson, S. Eger, V. Murcia, H. Ade, B. A. Collins, *J. Phys. Chem. C* **2017**, *121*, 21720.
- [45] M. Böckmann, T. Schemme, D. H. De Jong, C. Denz, A. Heuer, N. L. Doltsinis, *Phys. Chem. Chem. Phys.* **2015**, *17*, 28616.
- [46] D. Raithel, L. Simine, S. Pickel, K. Schötz, F. Panzer, S. Baderschneider, D. Schiefer, R. Lohwasser, J. Köhler, M. Thelakkat, M. Sommer, A. Köhler, P. J. Rossky, R. Hildner, *Proc. Natl. Acad. Sci. USA* **2018**, *115*, 2699.
- [47] J. Jakowski, J. Huang, S. Garashchuk, Y. Luo, K. Hong, J. Keum, B. G. Sumpter, *J. Phys. Chem. Lett.* **2017**, *8*, 4333.
- [48] A. Maillard, A. Rochefort, *Phys. Rev. B* **2009**, *79*, 115207.
- [49] T. Tsumuraya, J.-H. Song, A. J. Freeman, *Phys. Rev. B* **2012**, *86*, 075114.
- [50] N. Banerji, S. Cowan, E. Vauthey, A. J. Heeger, *J. Phys. Chem. C* **2011**, *115*, 9726.
- [51] D. M. Delongchamp, R. J. Kline, D. A. Fischer, L. J. Richter, M. F. Toney, *Adv. Mater.* **2011**, *23*, 319.
- [52] X. Lu, H. Hlaing, D. S. Germack, J. Peet, W. H. Jo, D. Andrienko, K. Kremer, B. M. Ocko, *Nat. Commun.* **2012**, *3*, 795.
- [53] A. I. Abdul Hapip, F. Abd. Wahab, K. Sulaiman, *Mater. Res. Innovations* **2011**, *15*, s198.
- [54] G. V. Naik, J. L. Schroeder, X. Ni, A. V. Kildishev, T. D. Sands, A. Boltasseva, *Opt. Mater. Express* **2012**, *2*, 478.
- [55] A. Ciesielski, L. Skowronski, M. Trzcinski, T. Szoplík, *Appl. Surf. Sci.* **2017**, *421*, 349.
- [56] D. I. Yakubovsky, A. V. Arsenin, Y. V. Stebunov, D. Y. Fedyanin, V. S. Volkov, *Opt. Express* **2017**, *25*, 25574.
- [57] G. Kresse, J. Hafner, *Phys. Rev. B* **1993**, *47*, 558.
- [58] M. Gajdoš, K. Hummer, G. Kresse, J. Furthmüller, F. Bechstedt, *Phys. Rev. B* **2006**, *73*, 045112.
- [59] J. Heyd, G. E. Scuseria, M. Ernzerhof, *J. Chem. Phys.* **2003**, *118*, 8207.